analytical chemistry

pubs.acs.org/ac Article

Dual-Channel Microfluidic Photoionization Detector

Anjali Devi Sivakumar, Ruchi Sharma, Junqi Wang, Weiliang Liang, Yulong Zhou, and Xudong Fan*

Cite This: *Anal. Chem.* 2025, 97, 22397−22406 Read Online

ACCESS | Metrics & More | Article Recommendations | Supporting Information

ABSTRACT: Microfluidic photoionization detectors (μPIDs) have long served as a highly sensitive gas sensor in a microgas chromatography (μGC) device. However, their high electrical impedance renders them susceptible to various noise sources, often hindering their performance and bandwidth. Here, we developed a silicon-based, microfluidic differential dual-channel photoionization detector (μDPID) to reject common-mode noises and enhance operational reliability under varying environmental conditions. Comprehensive analyses of the μDPID were conducted by benchmarking its performance against the corresponding μPID configuration for different noise sources. Experimental results demonstrate that the μDPID significantly enhances noise immunity, providing a linear dynamic range of ∼2 × 10^5 (from 38.5 nA to 0.21 pA) at a large bandwidth of 106 Hz. These advancements underscore the μDPID's potential for developing high-performance μGC systems such as portable ultrafast GC and comprehensive 2-dimensional GC for rapid, in situ trace vapor detection.

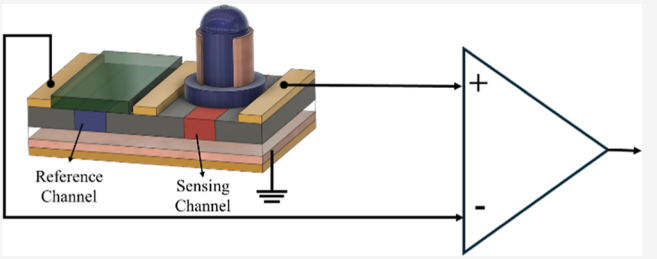

INTRODUCTION

Rapid in situ vapor analysis has become increasingly important across various sectors, including healthcare,[1−8] environmental surveillance,[9−11] space exploration,[12] and food safety.[13−15] Microgas chromatography (μGC)[1,2,9,14,16,17] is extensively used for these applications due to its ability to identify a broad range of gases and compact size. Various miniaturized gas detectors (summarized in Table S1) have been developed for use with μGC. Among these, the microfluidic photoionization detector (μPID)[16−20] is especially popular because of its fast response, high sensitivity, simple manufacturing, and low power requirements.[16,18,20,21]

We previously developed a silicon chip-based microfluidic μPID,[16,18] which has a small ionization chamber volume (5−7 μL) and a flow-through structure (i.e., nearly zero dead volume). When used in GC, a detection limit of a single-digit ppt (in 1 L of sample) has been achieved.[16,18] However, compared to other microgas detectors listed in Table S1, this μPID is a high-impedance (on the order of GΩ to TΩ) current source, making it particularly vulnerable to various noise sources summarized in Table S2. Unfortunately, some of these noises, such as ambient-coupled noise and electromagnetic interference (EMI) noise[22] cannot be mitigated solely by using expensive and bulky benchtop electrometers, which are often impractical for use in portable field applications.

Although using low-pass filters helps dampen some of these noises, as used in our previous designs[16,18] (0.68 mV noise with a benchtop amplifier at a 10 Hz cutoff frequency and 0.016 mV noise with an in-house developed circuit at a 1.5 Hz cutoff frequency), the variability of the noise sources often reduces the efficiency of these filters. Additionally, adding a filter significantly reduces the speed of the μPID, which limits the μPID's use in ultrafast GC[23,24] and comprehensive 2-dimensional GC[25,26] that has a subsecond peak width in second-dimensional separation. To increase bandwidth while minimizing noise, here we introduce a microfluidic differential dual-channel μPID (μDPID) with an on-chip heater shown in Figure 1A. It features two microfabricated channels on the same silicon chip: one functions as a standard μPID (the "sensing channel"), and the other as a reference (the "reference channel"). This differential design greatly suppresses common-mode noises, leading to a bandwidth of 106 Hz and a linear dynamic range of ∼2 × 10^5 (from 3.85 V to 0.021 mV or 38.5 nA to 0.21 pA) without additional signal processing.

MATERIALS AND METHODS

Materials. P-type/boron prime silicon (Si) wafers (100 mm in diameter, 400 μm thick, 0.001−0.005 Ω cm, double-sided-polished (DSP)) were from Ultrasil. Borofloat 33 Pyrex glass wafers (P/N: 517) were from University Wafer. Kr VUV lamp (P/N: 043-257) and piD-TECH eVx Red Label (0−200 ppm) Plug-In PID Sensor (P/N: 045-012) were from MOCON (part of AMETEK). INA121 Instrumentation Amplifier (P/N: INA121P) was from Texas Instruments. ADS1262 32-bit precision Sigma Delta ADC breakout board

Received: August 15, 2025
Revised: September 25, 2025
Accepted: September 26, 2025
Published: October 2, 2025

https://doi.org/10.1021/acs.analchem.5c05021
Anal. Chem. 2025, 97, 22397−22406

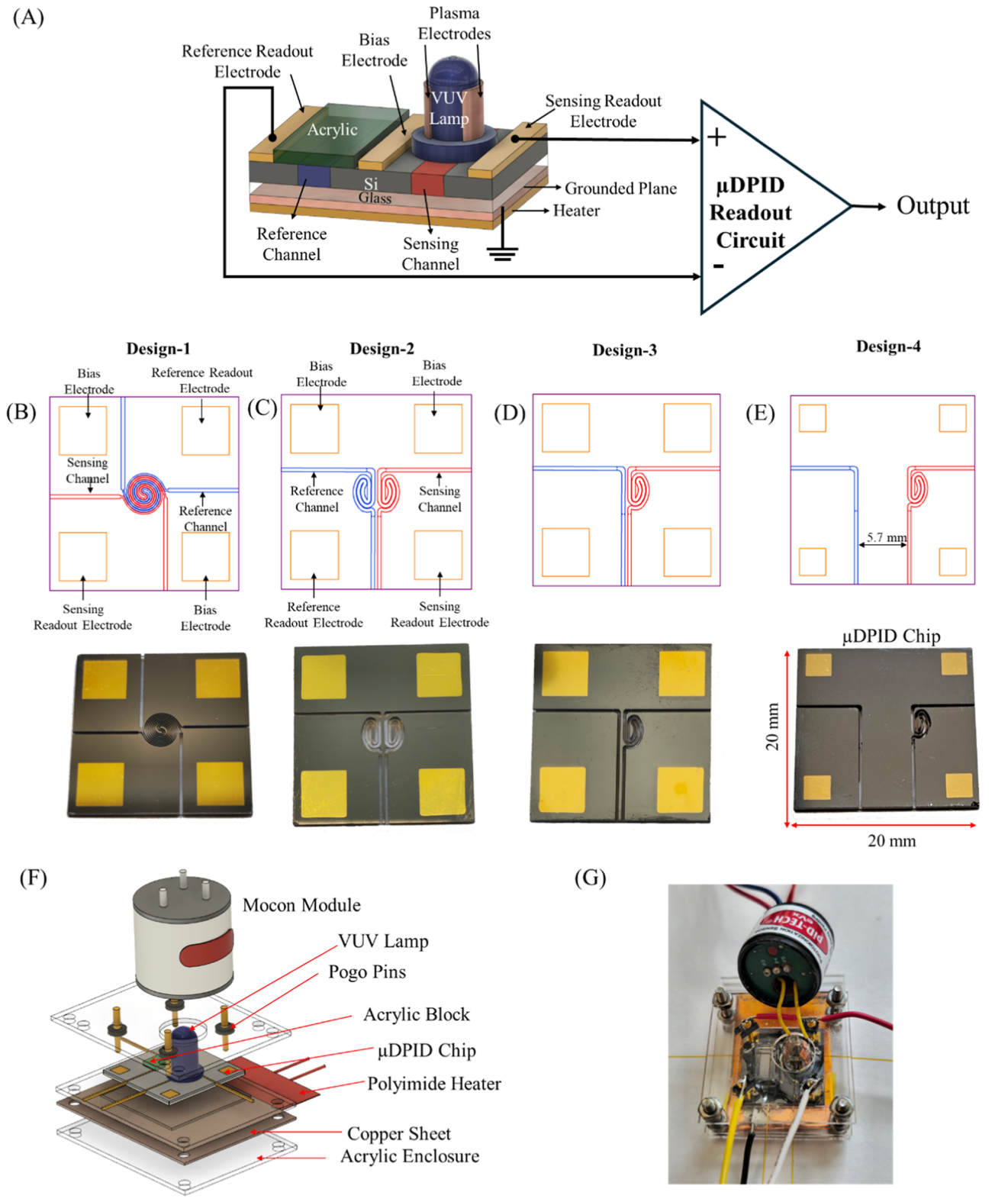

Figure 1. (A) μDPID device consisting of a μDPID module, an associated readout circuit, and an auxiliary power supply circuit (not shown). (B–E) Four μDPID designs explored in this work: (B) Co-spiral channels. (C) Side-by-side spiral channels. (D) Straight-spiral channels side-by-side. (E) Straight-spiral channels with a spacing of ~5.7 mm. Design-1 and Design-2 are geometrically symmetrical. Design-3 and Design-4 are geometrically asymmetrical, since the reference and sensing channels have different shapes. The blue channel and red channel in the top panel denote the reference and sensing channels, respectively. The corresponding specifications of these four designs are listed in Table S3. (F) Exploded view of a μDPID module using a Design-4 chip. (G) Corresponding photo. Note that the Mocon module is intentionally tilted to show the VUV lamp underneath.

https://doi.org/10.1021/acs.analchem.5c05021
Anal. Chem. 2025, 97, 22397−22406

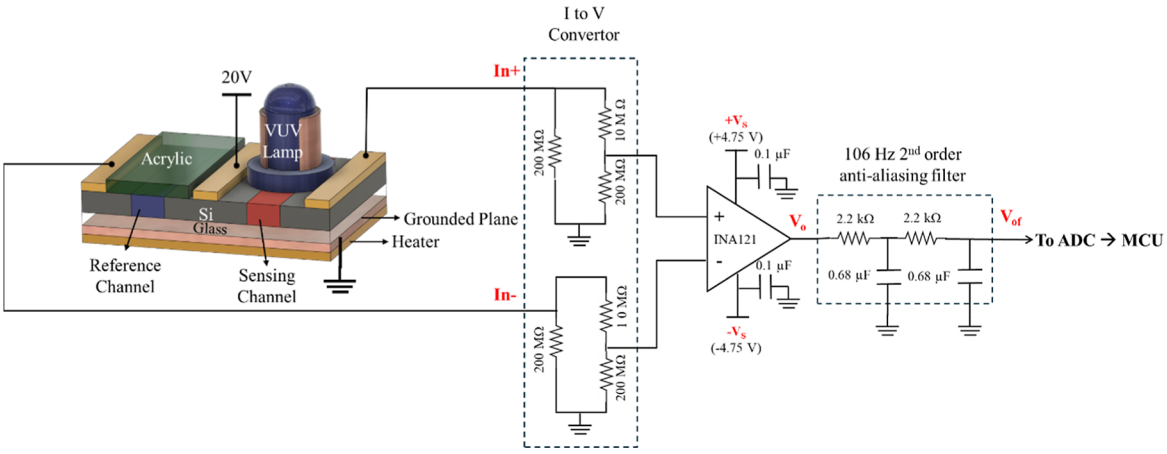

Figure 2. μDPID readout circuit.

(P/N: PC-4143) was from Protocentral Electronics. Seeeduino XIAO NRF52840 SENSE—Microcontroller Unit (MCU) (P/N: 102010469) was from Seeed Technology Co., Ltd. Solid State Relay (SSR), CS326 was from Coto Technology. Polyimide Flexible Heater (P/N: PLMLV-101/10) was from Dwyer Instruments, LLC. 1/16″ thick (P/N: 8560K178), 1/8″ thick (P/N: 8560K199) Clear Scratch- and UV-Resistant Cast Acrylic Sheet, and 0.025″ thick Super-Conductive 101 Copper Sheet (P/N: 89675K713) were from McMaster-Carr. 0.004″ thick Conductive Copper Foil Adhesive Tape (P/N: 1067−1126−2−6-ND) was from DigiKey. UV-curable epoxy (P/N NOA 68T) was from Norland Products. Pogo pins were from Adafruit (P/N: 5381). Adafruit USB Isolator was (P/N: 2107) from Adafruit. Benzene (P/N: 270709-1L), Chlorobenzene (P/N: 23570-250 ML), and o-Xylene (P/N: 95662-250 ML) were from Sigma-Aldrich.

μDPID Chip Fabrication. The fabrication process of the μDPID chips is shown in Figure S1, which is adapted from the fabrication of our previous μPID chip in 16,18. First, silicon and glass wafers were cleaned with a nanostrip solution, and then they were anodically bonded at 350 °C under vacuum. After bonding, the bonded wafer was cleaned again with the nanostrip solution to remove contaminants from the bonding chuck. A layer of photoresist (PR) was then patterned on the silicon side for deep reactive ion etching (DRIE) on silicon. Si was etched down completely (400 μm deep) using DRIE to create microfluidic channels for the photoionization detector. The PR remaining on the silicon surface was then subjected to O_2 plasma cleaning to strip any remaining organics and remove any hardened PR residues on the silicon surface caused by the DRIE process. This was followed by deposition of Cr/Au on the silicon through an evaporation process using a silicon shadow mask to form the electrodes of the photoionization detector. Ion milling was also performed before metal evaporation on the silicon surface to remove any native oxide, enhancing the ohmic contact of the electrodes. Finally, the wafer was diced into ∼20 mm × 20 mm pieces (see Figure 1B−E, bottom panel). Four designs of the μDPID chips were made, and their corresponding channel cross sections and lengths are given in Table S3.

μDPID Packaging. For a fully packaged μDPID module depicted in Figure 1F,G, the top surface of the sensing and reference channels of the Design-4 μDPID chip (Figure 1E) was sealed with a VUV lamp and a laser-cut acrylic block, respectively, using UV-curable epoxy. Guard columns were inserted into the fluidic ports of both the sensing and reference channels for the fluidic connection. A MOCON piD-TECH module was used to excite the plasma in the VUV lamp through conductive copper tape affixed to the VUV lamp electrodes.

All the electrical connections to the μDPID chip were achieved via spring-loaded pogo pins affixed to a laser-cut acrylic enclosure. Figure 1F,G show the exploded view and a photo of the final packaged μDPID module, respectively. Note that the carrier gas (such as helium or nitrogen) and analytes flow through the sensing channel during actual operation. The reference channel can be filled with either carrier gas or ambient air. However, flowing carrier gas through the reference channel is more complicated (since it requires an additional connection to the carrier gas) and consumes additional gas. Therefore, in this paper, we simply let the reference channel be filled with ambient air.

Experimental Setup for μDPID as GC Detector. To evaluate the performance of the μDPID at 23 °C (room temperature) and 50 °C, we chose Benzene (C_6H_6, boiling point: 80.1 °C, ionization potential: 9.25 eV), Chlorobenzene (C_6H_5Cl, boiling point: 132 °C, ionization potential: 9.07 eV), and o-Xylene (C_8H_{10}, boiling point: 144 °C, ionization potential: 8.56 eV) as model systems. Gas samples for these analytes were collected from the headspace of screw-thread vials using a gastight syringe, then injected into the injector of the HP 6890 series GC System, which operated at 300 °C with a split ratio of 30, using helium as the carrier gas. The injection port outlet was connected to the μDPID's sensing channel via a 34-in. guard column, while its reference channel was left open to the ambient. The other end of the μDPID's sensing channel was connected to the Flame Ionization Detector (FID) in the HP 6890 through a 29-in. guard column. Both the 34-in. and 29-in. guard columns were maintained at room temperature. The flow rate at the inlet of the FID was set to ∼1 mL/min. The FID was set to operate at 250 °C, with a hydrogen flow rate of 40 mL/min and a dry air flow of 200 mL/min. Note, here we used the FID as a reference detector to characterize the μDPID at 23 and 50 °C. The data sampling rate of FID was set to 100 Hz, and the μDPID module signal bandwidth was set to 106 Hz. To monitor the thermal cycling performance of the μDPID module with the VOCs detection, data were initially obtained at 23 °C for #1−23 °C. The module was then heated for approximately 15 min to reach

https://doi.org/10.1021/acs.analchem.5c05021
Anal. Chem. 2025, 97, 22397−22406

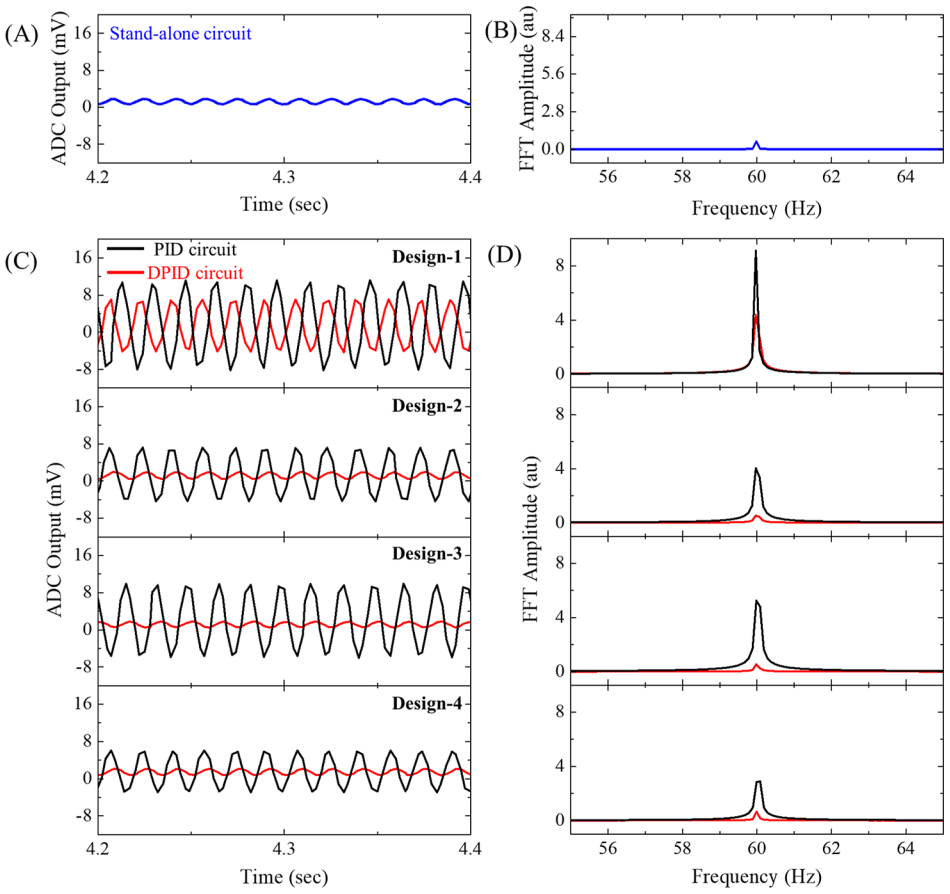

Figure 3. Ambient-coupled noise analysis of μDPID chip designs with the circuit configuration shown in Figure S5 without a Faraday cage. (A) ADC output snippet for the standalone readout circuit. (B) Corresponding FFT spectrum. (C) ADC output snippets for both the μDPID circuit (red) and the μPID circuit (black). (D) Corresponding FFT spectra. All the noise values are tabulated in Table S6. All the signals were recorded with a bandwidth of 106 Hz for 10 s at 23 °C. All the characterizations were performed with the μDPID chip sandwiched between laser-cut acrylic sheets with the electrodes exposed.

around 50 °C to collect #2−50 °C data. Afterward, it was cooled back to 23 °C before recording the #3−23 °C.

RESULTS AND DISCUSSION

The main components of a μDPID device (depicted in Figure 1A) are a μDPID module, consisting of a microfluidic chip and a vacuum ultraviolet (VUV) lamp, and a readout circuit, as well as an auxiliary power supply circuit, as described as follows.

μDPID Module Design. A conventional μPID[16,18,20] chip consists of a single microfluidic channel (e.g., Archimedean spiral design in our previous work[16,18]) with the two facing walls forming electrodes to collect electrons and ions under a bias voltage.[18] In contrast, the μDPID chip has two channels: a sensing channel and a reference channel. Gas detection occurs in the sensing channel with a VUV lamp on top. We examined four different μDPID chip designs in Figure 1B−E. The μDPID Chip Fabrication section discusses the methodology used for fabricating these chips.

To operate the μDPID module at a higher temperature (50 °C in the current work), a polyimide heater (refer to Figure 1A,F) was mounted on the back of the μDPID chip, with an intermediate grounded copper sheet insulated with Kapton tape (referred to as a "grounded plane"—see Figure 1A). As explained later, this setup shields the μDPID chip from EMI caused by heater pulse width modulation (PWM). Although the current design utilizes an off-the-shelf heater, both the grounded plane and heater can also be integrated into the μDPID chip during the microfabrication process, thereby eliminating the need for manual assembly. Figure 1F,G show the components in the μDPID module and the corresponding photo, respectively. The μDPID Packaging section describes the details of the assembly processes.

μDPID Readout Circuit Design. Figure 2 illustrates the readout circuit design for the μDPID. A μDPID chip comprises three electrodes (shown in Figure 1A): sensing readout, reference readout, and bias electrodes. Both the sensing and reference channels utilized the same bias electrode, to which a 20 V was applied. The sensing and reference readout electrodes were connected to the "In+" and "In−" terminals of the readout circuit, respectively. The currents produced by the sensing and reference channels were converted into voltage through a simple symmetric resistive network (equivalent resistance of ∼100 MΩ ± 1%) constructed at the INA121 inputs for efficient common-mode rejection. This I to V conversion method is preferred over a transimpedance amplifier to prevent extra noise from entering the circuit. For maximal dynamic range, the INA121 was powered by a ±4.75 V bipolar voltage supply (see Section S5 for details on the choice of the amplifier voltage supply and the linearity test).

The output signal (V_{of}) from INA121 was subsequently fed to a 32-bit Analog-to-Digital Converter (ADC). To prevent

https://doi.org/10.1021/acs.analchem.5c05021
Anal. Chem. 2025, 97, 22397−22406

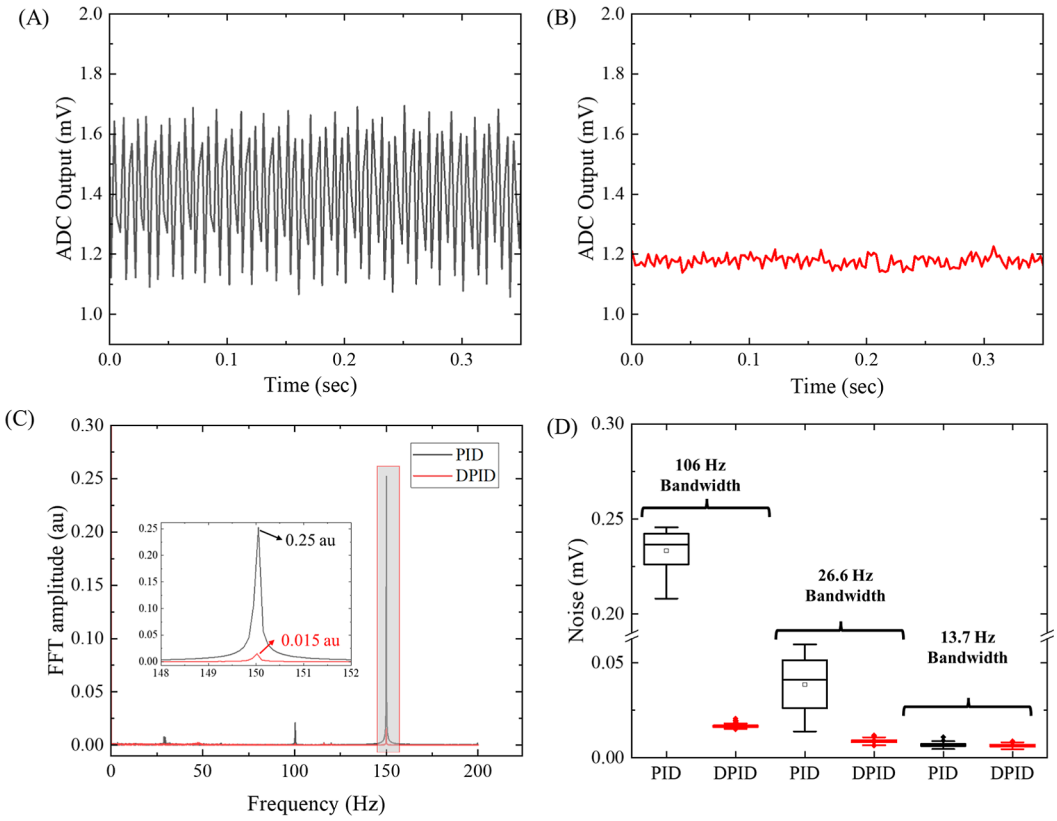

Figure 4. Heater-induced noise in a μDPID chip. (A,B) 0.35 s snippets of μPID (black) and μDPID (red) signals, respectively, from Figure S12A recorded for 600 s with a 106 Hz bandwidth using the Design-4 μDPID chip with the on-chip heater turned ON. (C) Corresponding FFT spectra of the μPID and the μDPID signals. The 150 Hz heater-related EMI FFT amplitude detected by the μPID and the μDPID is 0.25 and 0.015, respectively. (D) Noise distribution in the μPID (black) and μDPID (red) signal operated at 106, 26.6, and 13.7 Hz bandwidth with the heater ON for 600 s. The corresponding noise analysis is shown in Figure S12(D). The μPID and μDPID data were collected with an on-chip heater in the μDPID chip operated by a unipolar 16 V, 150 Hz, and 80% duty cycle PWM signal. The heater was activated just immediately before the start of data collection. The initial temperature at t = 0 s was approximately 23 °C (room temperature) for all the bandwidths. All the characterizations were performed with the μDPID chip sandwiched between laser-cut acrylic sheets with the electrodes exposed.

aliasing of unwanted high-frequency signals sent to the ADC, a second-order low-pass antialiasing RC filter with a cutoff frequency of 106 Hz was implemented to assist the built-in digital Sinc filter in the ADC. This RC filter uses a small resistor (~2.2 kΩ) to minimize signal offsets and decrease additional noise resulting from any leakage currents from the ADC input. In this work, the bandwidths used were 106, 26.6, and 13.7 Hz (see Section S6 for details on the ADC settings).

Finally, a microcontroller unit (MCU) was employed to collect the digitized ADC signal via SPI communication. The ADC data collected by the MCU was then streamed in real time to the LabVIEW program on the laptop via wired USB communication. A USB isolator was used to avoid unwanted noise, including 60 Hz power line interference injected into the μDPID device through this USB communication. Section S7 describes the overall architecture for the μDPID device.

Batteries, instead of a wall-mounted AC supply, were preferred for use with the μDPID to avoid 60 Hz power line noise. Moreover, using batteries for portable applications is also simpler and more practical. Given the μDPID's low power consumption (180 mW, due mainly to plasma excitation), a 16 V, 5000 mAh battery could last up to ~19 days of continuous operation without the heater being activated. With the μDPID heater activated (<3 W for 50 °C), the batteries can last ~30 h.

Finally, the entire readout circuit, along with the μDPID module, was enclosed in a solid Faraday cage made up of a laser-cut acrylic box covered with adhesive conductive copper foil tape for reduced weight and improved thermal insulation (see Figure S3A).

Note that the μDPID can be converted to a regular μPID, i.e., our previous version reported in 16,18 by disconnecting the reference electrode from the "In−" of the readout circuit. This allows us to test the regular μPID under otherwise identical conditions for comparison.

Readout Circuit Noise and Baseline Offset. As mentioned previously in Table S2, the μDPID readout circuit (Figure 2), designed to amplify the μDPID signal, also contributes considerable noise resulting from both voltage and current noise from the amplifier and thermal noise from various circuit components, including resistors and the amplifier. Section S8 provides a detailed noise analysis of the μDPID's readout circuit. Table S5 summarizes the noise comparison of the readout circuit with the instrumentation amplifiers employed in both the previous[16,19] and the current work, showing that INA121 used in the current work produces much lower noise than INA122 used previously,[16,19] which results from the lower current noise of ~1 fA/Hz$^{1/2}$ produced by INA121 than ~80 fA/Hz$^{1/2}$ by INA122. Furthermore, Table S5 indicates that the predominant noise source in the current INA121-based readout circuit is the thermal noise (1.26 μV/Hz$^{1/2}$) generated by the 100 MΩ resistor used for amplifying the current (in the pA range) from the μDPID.

https://doi.org/10.1021/acs.analchem.5c05021
Anal. Chem. 2025, 97, 22397−22406

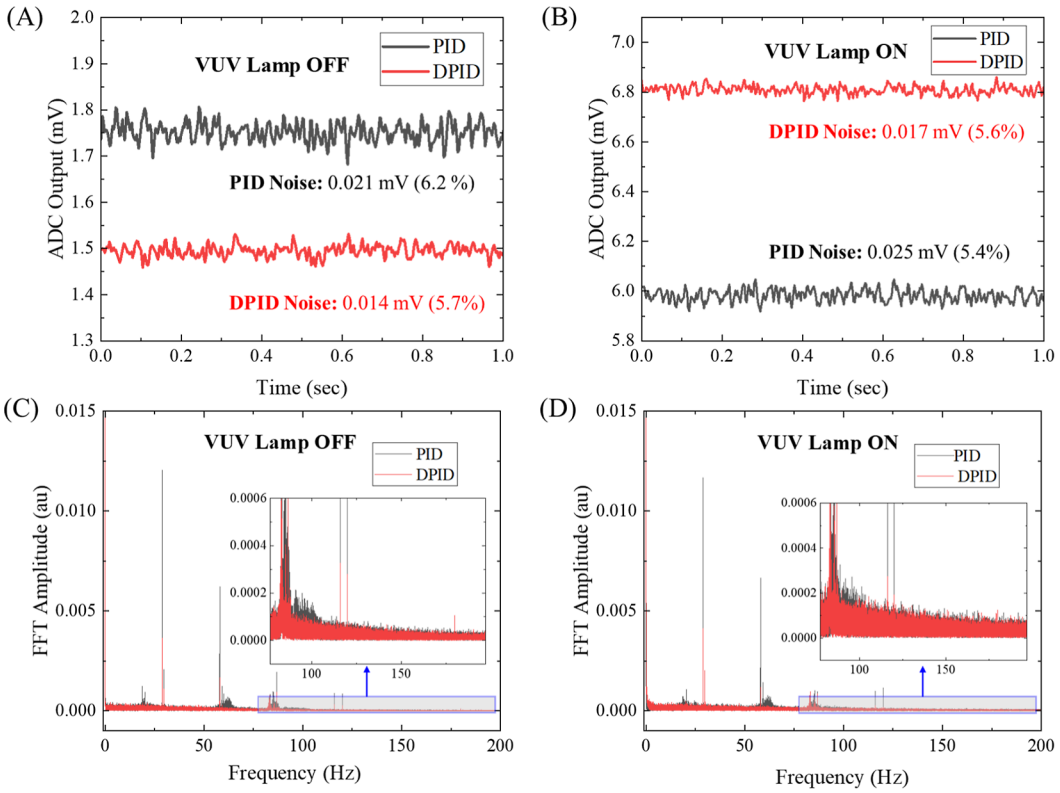

Figure 5. Contribution of plasma excitation-induced noise. (A,B) 1 s snippet of μPID (black) and μDPID (red) signals recorded with the VUV lamp OFF and VUV lamp ON, respectively, from Figure S15 for 300 s. Notably, the baseline of both signals in (B) increases by 4.3 mV for μPID and 5.3 mV for μDPID when the VUV lamp is ON. (C,D) Corresponding FFT spectra. The insets in (C,D) provide zoomed-in views of the shaded areas. All μDPID and μPID signals were recorded with a bandwidth of 106 Hz at 23 °C. Helium gas was flowed at a rate of 3 mL/min in the sensing channel of the μDPID, whereas the reference channel was left open to the ambience.

Table 1. Comparison of the Noise Levels of μDPID and μPID Recorded Over a Duration of 300 s at Different Bandwidths (106, 26.6, and 13.7 Hz), for Conditions: VUV Lamp OFF and Heater OFF, VUV Lamp ON but Heater OFF, and Both VUV Lamp and Heater ON[a]

setup	bandwidth (Hz)	noise with heater OFF (mV)		noise with heater ON (mV)
		VUV lamp OFF	VUV lamp ON	VUV lamp ON
μPID	106	0.021 (6.2%)	0.025 (5.4%)	0.2 (2.0%)
	26.6	0.012 (8.2%)	0.013 (8.4%)	0.03 (34.4%)
	13.7	0.0076 (8.4%)	0.0076 (9.8%)	0.0065 (11.0%)
μDPID	106	0.014 (5.7%)	0.017 (5.6%)	0.021 (3.1%)
	26.6	0.009 (9.7%)	0.0099 (9.3%)	0.01 (9.1%)
	13.7	0.0067 (10.7%)	0.0069 (13.3%)	0.0066 (11.3%)

[a]The snippets of the μPID and μDPID raw data are provided in Figures S15 and S16. The noise reported is for one standard deviation. The visual statistical representation of the noise presented in this table is depicted in Figure S17.

Additionally, the amplifier's input bias current can lead to a significant output signal offset. The INA121 amplifier has a much lower input bias current (~50 pA) than ~25 nA in INA122, which helps minimize this offset (~5 mV—see Table S5) and eliminates the external offset tuning circuitry in the prior work.[16,19]

μDPID Chip Ambient-Coupled Noise Characterization. The μDPID is a high-impedance current source (on the order of TΩ—see Table S3), and the amplifier used in the μDPID readout circuit also has a very high input impedance (1000 GΩ—see Table S5). These points are highly sensitive to electrostatic and inductive coupling with nearby interference sources.[27] However, due to the high impedance nature of the μDPID, electrostatic coupling is more dominant than the inductive coupling.[28] These electrostatic couplings for μDPID with ambient sources can reach up to sub-nF.[28,29] As a result, multiple sources may collectively raise the coupling capacitance to nearly sub-μF levels.

The effect of these ambient electrostatic couplings in all four μDPID chips was first examined without any shielding mechanism (such as a Faraday cage) and no heater installed, using three circuit configurations: standalone readout circuit (Figure S5A), μDPID circuit (Figure S5B), and μPID circuit (Figure S5C). The impact of the electrostatic coupling in these circuits is demonstrated in Figure 3, showing the dominant 60 Hz noise picked up by all four chip designs from the nearby devices. In all four designs, the noise in the μDPID circuit was significantly lower than in the μPID circuit due to the common-mode noise rejection feature built into the μDPID (see Figure 3C and Table S6). However, the Design-1 μDPID circuit exhibited substantially higher noise than the other three designs. We speculate that this design may be more susceptible to environmental changes, as it has a lower resistance between two electrodes compared to other designs (see Table S3) due

https://doi.org/10.1021/acs.analchem.5c05021
Anal. Chem. 2025, 97, 22397−22406

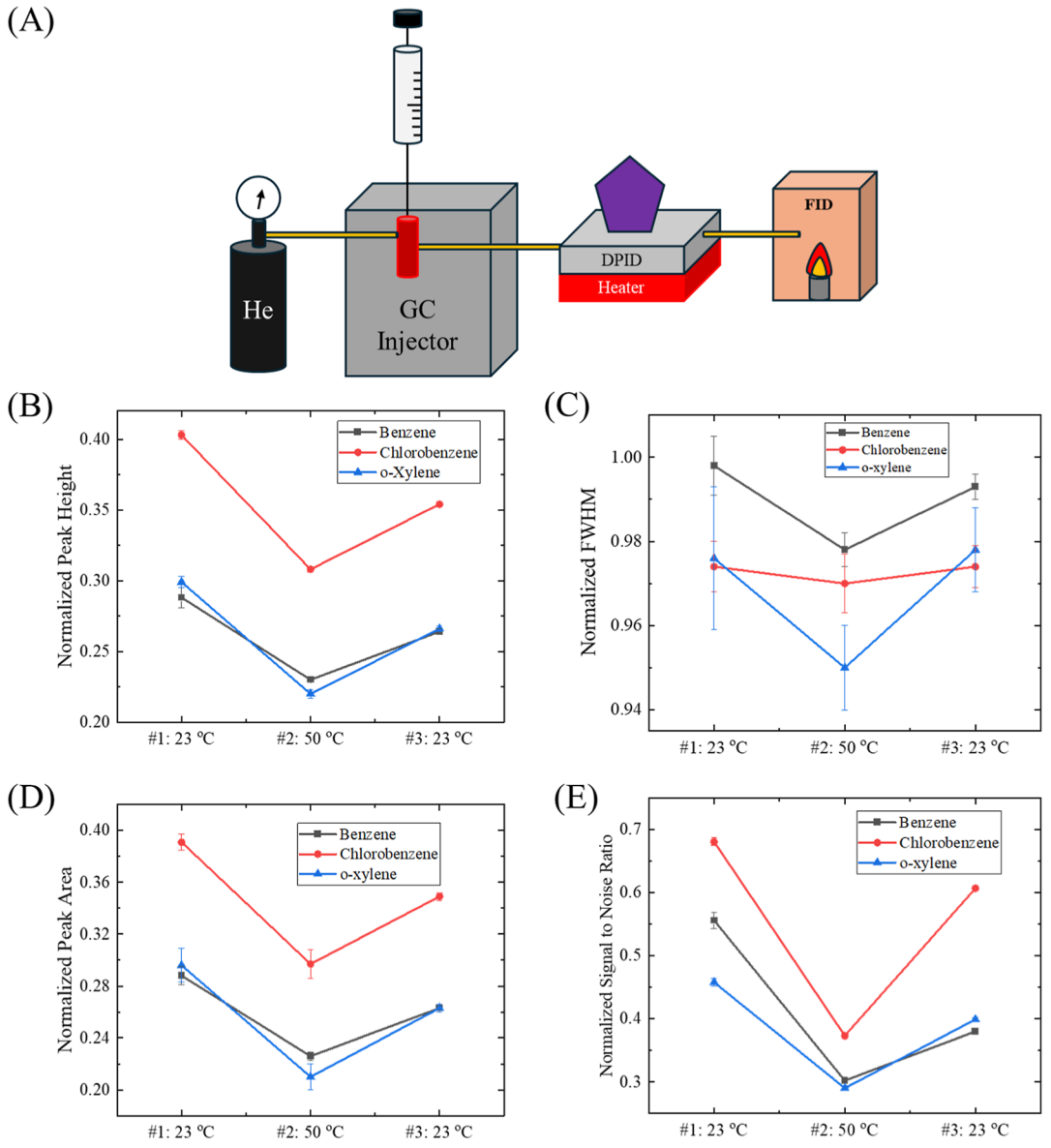

Figure 6. Characterization of μDPID with standard gas models (such as benzene, chlorobenzene, and o-xylene) at 23 and 50 °C. (A) The experimental setup used for testing the μDPID with standard gas. The FID detector on the benchtop GC connected in series with the μDPID sensing channel served as a reference to compare the performance of the μDPID at 23 °C (room temperature) and 50 °C. (B–E) Peak height, FWHM, peak area, and SNR of the gas peaks detected by the μDPID normalized to the corresponding FID data. Error bars are obtained with ∼10 measurements. The corresponding chromatogram is shown in Section S17, and Table S9 summarizes the parameters of the peaks detected by FID and μDPID. Here, #1−23 °C indicates gas detection at t = 0 s when the μDPID temperature was 23 °C. #2−50 °C signifies gas detection after heating the μDPID module for ∼15 min to reach ∼50 °C, with 80% PWM applied to the heater. #3−23 °C represents gas detection after cooling the μDPID back to 23 °C.

to the narrower gap (160 μm) and longer channel (50 mm), which results in a higher leakage current.[30] On the other hand, in Designs 2, 3, and 4, the noise in the μDPID circuit was similar to that in the standalone readout circuit. However, the standalone readout and μDPID circuit still exhibited some residual common-mode 60 Hz noise as noted in Figure 3, which may be attributed to resistance mismatch between the sensing and reference channels in the μDPID chip and/or in the resistive network at the input of IN121.

To further reduce the noise, the performance of the three circuits was evaluated by enclosing them inside a grounded solid Faraday cage (Figure S3A). From Figure S6A,C, it is evident that the noise of all circuits decreases significantly compared to their counterparts in Figure 3A,C. Additionally, the FFT spectrum in Figure S6D shows that even with a Faraday cage, the μPID circuit still exhibits electrostatic coupling at multiple frequencies. This electrostatic coupling at the μPID circuit might be related to the efficiency of the Faraday cage, as studies have shown that, depending on the Faraday cage design, it may not fully attenuate coupling noises, due primarily to the conductivity of the Faraday cage metal, joints, gaps, probes, and fluidic openings in the cage.[31] These Faraday cages may allow moisture to enter, increasing stray coupling. In contrast, the μDPID dampened them (see Figure S6D) even with the above limitations, making it suitable for measuring currents as low as pA.

We further evaluated the long-term stability of the circuits (see Table S7). Although the noise in the μPID circuits

https://doi.org/10.1021/acs.analchem.5c05021
Anal. Chem. 2025, 97, 22397−22406

fluctuates, the noise in the μDPID circuits remains relatively stable over 2 days, highlighting the advantage of the μDPID. An exception is the Design-1 μDPID circuit, which shows a 93% increase in noise (while the Design-1 μPID circuit experiences roughly a 520% increase). This may be due to the lower channel resistance of Design-1 compared to other designs (see Table S3), causing leakage currents in the μDPID chip as observed in Figure 3 and Table S6. Additionally, comparing the noise levels of the other three designs (Design-2, Design-3, and Design-4) in Table S7, it appears that regardless of their symmetry, μDPID circuits exhibit similar noise levels, likely because of their high channel resistance (see Table S3). Therefore, from now on, we will focus solely on Design-4 (shown in Figure 1E), enclosed in a Faraday cage (depicted in Figure S3A) for the subsequent sections, due to its simplicity and better fluidic isolation between the sensing and reference channels.

μDPID Chip Heater and Temperature Related Noise Characterization. Moisture and volatile organic compounds (VOCs) condensation and accumulation on the VUV lamp window and PID electrodes are common issues in PID sensors, causing leakage currents and significantly reduced sensitivity. Adding an on-chip heater can help mitigate this issue. It also helps produce narrower peak widths for heavier VOCs when used with a GC system.[18] However, adding an on-chip heater increases noise from higher operating temperatures and EMI caused by the heater's PWM. Among these, EMI noise is the most significant. Section S10 shows the effect of heater PWM-induced EMI on the μPID (or μDPID) signal using COMSOL. Additionally, methods to reduce this interference, such as positioning the heater farther from the detector, adding a grounded plane, using a high-frequency PWM, using an analog heater control, and other strategies, are examined in Section S11 and summarized in Table S8.

Our μDPID included an on-chip heater integrated with a grounded plane (copper sheet in Figure 1F) and operated at a PWM frequency of 150 Hz. Performance tests comparing the μDPID and the μPID with the heater ON show that the μPID detects a significant amount of 150 Hz EMI noise from the heater PWM, whereas μDPID only detects a trace level of this noise at a 106 Hz signal bandwidth (see Figure 4A−C). Remarkably, the noise in the μDPID with the heater ON is just ∼0.017 mV, >10 times lower than the ∼0.24 mV in the μPID at the same bandwidth (see Figure 4D). The μDPID and μPID noise levels were also assessed at reduced bandwidths of 26.6 and 13.7 Hz (see Section S12). As expected, a lower noise was observed than at the 106 Hz bandwidth, as summarized in Figure 4D. Notably, the μPID displayed greater noise variations at 26.6 Hz than the μDPID, due to the 150 Hz heater PWM EMI being aliased at the 60 Hz ADC data sampling rate, as shown in Figure S12B. Additionally, Figures 4D and S12D indicate that the μPID with heater ON can achieve a low noise level (∼0.007 mV), similar to the μDPID, only at the lower bandwidth of 13.7 Hz (see Figure 4D). Conversely, the μDPID with the heater ON maintains a consistently low noise level (<0.02 mV) even at higher bandwidths of 106 and 26.6 Hz.

Furthermore, the temporal performance of the μPID and μDPID with the heater ON over 600 s, specifically during temperature ramping, was also examined at different bandwidths (see Section S12). Notably, at 106 Hz, the μPID clearly exhibited an increase in noise of ∼0.037 mV from t = 0 s at room temperature (23 °C) to 50 °C at t = 600 s, whereas the μDPID maintained a stable noise level over the entire 600 s.

Section S13 evaluates the impact of PWM duty on the μPID and μDPID noise. It was observed that the noise levels of both μDPID and μPID grow as the duty cycle increases, especially at the 106 Hz bandwidth. Nevertheless, the μDPID noise increased by only ∼0.01 mV, whereas the μPID noise rose by ∼0.25 mV when the PWM duty cycle increased from 10% to 60% at the 106 Hz bandwidth. Moreover, no significant noise increase was detected in the μDPID with duty cycle changes for bandwidths of 26.6 and 13.7 Hz, whereas the μPID showed no increase only at the lowest bandwidth of 13.7 Hz.

μDPID Device Characterization. All μDPID characterizations performed thus far did not involve a VUV lamp or plasma generation. The μDPID shown in Figure 1F,G employs a commercial Mocon circuit (∼960 V peak-to-peak sinusoidal output at ∼108 kHz—see Figure S14) to power the VUV lamp. Plasma generation usually produces two kinds of noise: shot (white) noise from plasma photons and EMI from the plasma excitation circuit.[22] In practice, shot noise is minimal compared to EMI noise, since the electrodes for high-voltage/frequency plasma generation are close to the μDPID. Consequently, shielding this EMI noise with a Faraday cage described earlier is impractical. Usually, this high-frequency noise appears as low-frequency harmonics in the μPID/μDPID signal because of signal aliasing caused by the low ADC data sampling rate (for instance, 400 Hz sampling rate for the 106 Hz bandwidth—see Table S4).

Figure 5A,B show the noise of the μPID and μDPID increased by about 0.004 mV and 0.003 mV, respectively, when the VUV lamp was ON (but the heater was OFF). The FFT spectra in Figure 5C,D reveal that the noise increase occurred uniformly across all frequencies, indicating a rise in broadband (white) noise, which may be caused by the addition of white noise into the μDPID's sensing channel (and μPID as well) from the VUV photons. However, despite broadband noise, comparison between Figure 5C,D shows that no additional prominent frequency noise component emerges when the VUV lamp is ON. This probably results from effective high-frequency filtering by the second-order 106 Hz low-pass filter and low EMI generated by the piezoelectric transformer used in the Mocon plasma generation circuit,[32] compared to a magnetic transformer[33] used in the prior work.[16] Note that the minimal noise increase (∼0.003 mV) also justifies our VUV lamp placement fully on the μDPID's sensing channel (as depicted in Figure 1A) for maximal usage of VUV photons, thereby maintaining the gas detection sensitivity reported in our previous work.[16,18] The μPID and μDPID noise was further evaluated at lower bandwidths of 26.6 and 13.7 Hz when the heater was OFF. Figure S15 shows that both the μPID and μDPID noise levels decrease as the signal bandwidth decreases, as expected. The combined effect of plasma ON and heater PWM ON for both the μPID and μDPID was investigated in Figure S16. All the noise values for all conditions, lamp OFF and heater OFF, lamp ON but heater OFF, and both lamp and heater ON, are summarized in Figure S17 and Table 1.

In Section S16, the temporal performance of both μPID and μDPID was also assessed when the heater was OFF and ON (and the VUV lamp remained ON) at a 106 Hz bandwidth. Figures S18C and S19C show that the μDPID's noise remained low and stable over time compared to the μPID. However, both μPID and μDPID exhibited a baseline drift of

https://doi.org/10.1021/acs.analchem.5c05021
Anal. Chem. 2025, 97, 22397−22406

~4 mV with temperature ramping (Figure S19B), compared to the constant baseline observed with the heater OFF (Figure S18B). However, the baseline for both μPID and μDPID stabilized once the target temperature (~50 °C) was reached.

Characterization of μDPID as GC Detector at 23 and 50 °C. The performance of the μDPID was further evaluated using benzene, chlorobenzene, and *o*-xylene as gas models, with the FID connected in series with the μDPID sensing channel serving as the reference. The detailed experimental setup is outlined in the section Experimental Setup for μDPID as Gas Detector and is visually represented in Figure 6A. Experiments were conducted at two μDPID temperatures, 23 °C (room temperature) and 50 °C. The corresponding raw data is provided in Section S17.

Analysis of Figure 6B,D reveals that both the normalized peak height and peak area for all gases decrease at 50 °C compared to 23 °C. This decline is likely attributable to the faster transit time of the gases through the channel at elevated temperatures, as evidenced by a reduction in the full width at half-maximum (FWHM) for these gases at 50 °C. Table S9 further indicates that the fwhm of the gases correlates positively with their boiling points: *o*-xylene exhibits the highest FWHM of ~2.3 s, whereas benzene shows the lowest of ~0.73 s. These values also decrease at 50 °C, as shown in Figure 6C. Notably, by increasing the flow rate to 3 mL/min, the FWHM of benzene decreased by 45% in the μDPID. (see Table S9 and Figures S20 and S23).

Additionally, from Figure 6E, the signal-to-noise ratio (SNR) decreases at #2−50 °C compared to #1−23 °C and #3−23 °C for all three gases. This decline may result from both the lower peak height and increased baseline noise when the heater is ON in the μDPID, as discussed earlier in Table 1. However, based on the SNR values at #1−23 °C and #3−23 °C, it appears that thermal cycling of the μDPID has minimal impact on the μDPID performance.

CONCLUSIONS

In this study, a μDPID was developed to enhance the operational bandwidth while simultaneously minimizing noise. A comprehensive evaluation of the μDPID's performance was conducted in comparison to the μPID configuration under various noise conditions, demonstrating that the μDPID can operate reliably at a bandwidth of 106 Hz with a linear dynamic range of ~2×10^5 (from 3.85 V to 0.021 mV or 38.5 nA to 0.21 pA) at a temperature ranging from 23 to 50 °C. These capabilities underscore the μDPID's significant potential in advancing portable ultrafast μGC and comprehensive two-dimensional μGC for field-deployable applications.

The overall noise level of the μDPID device is observed to be comparable to the intrinsic noise of the INA121-based readout circuit, which is primarily dominated by the thermal noise inherent to the 100 MΩ gain resistor. To further enhance the SNR, a larger gain resistor can be used. For instance, a 2 GΩ gain resistor, analogous to that employed in a transimpedance amplifier,[34] would augment the SNR by a factor of 4.5. Furthermore, a new electrometer amplifier sensitive to femtoampere can also be explored.[34] Finally, increasing the voltage supply in INA121 beyond the current level of 4.75 V can expand the maximum output voltage and hence the dynamic range.

ASSOCIATED CONTENT

Supporting Information

The Supporting Information is available free of charge at https://pubs.acs.org/doi/10.1021/acs.analchem.5c05021.

Micro-Gas detectors, noise sources for μPID, design and fabrication of μDPID Chips, μDPID device architecture, and characterization, strategies to reduce heater PWM-related EMI, characterization of μDPID as GC detector (PDF)

AUTHOR INFORMATION

Corresponding Author

Xudong Fan − *Biomedical Engineering Department, University of Michigan, Ann Arbor, Michigan 48109, United States; Max Harry Weil Institute for Critical Care Research and Innovation and Center for Wireless Integrated MicroSensing and Systems (WIMS²), University of Michigan, Ann Arbor, Michigan 48109, United States;* orcid.org/0000-0003-0149-1326; Email: xsfan@umich.edu

Authors

Anjali Devi Sivakumar − *Biomedical Engineering Department, University of Michigan, Ann Arbor, Michigan 48109, United States; Electrical and Computer Engineering Department, Max Harry Weil Institute for Critical Care Research and Innovation, and Center for Wireless Integrated MicroSensing and Systems (WIMS²), University of Michigan, Ann Arbor, Michigan 48109, United States*

Ruchi Sharma − *Biomedical Engineering Department, University of Michigan, Ann Arbor, Michigan 48109, United States; Max Harry Weil Institute for Critical Care Research and Innovation and Center for Wireless Integrated MicroSensing and Systems (WIMS²), University of Michigan, Ann Arbor, Michigan 48109, United States;* orcid.org/0000-0002-3604-9784

Junqi Wang − *ChromX Health Co., Ltd, Guangzhou 510555, China*

Weiliang Liang − *ChromX Health Co., Ltd, Guangzhou 510555, China*

Yulong Zhou − *ChromX Health Co., Ltd, Guangzhou 510555, China*

Complete contact information is available at: https://pubs.acs.org/10.1021/acs.analchem.5c05021

Notes

The authors declare the following competing financial interest(s): X.F. is an inventor of the microfluidic photoionization detector technology that is related to the device described in this article. This technology is licensed to Nanova Environmental, Inc., ChromX Health Co., Ltd, and RUA Diagnostics, in which X.F. has financial interest.

ACKNOWLEDGMENTS

The authors thank ChromX Health Co., Ltd for the financial support. The authors acknowledge the Lurie Nanofabrication Facility for aid in microfabrication, and the University of Michigan Biomedical Engineering Design Spaces for aid in laser cutting.

REFERENCES

(1) Sharma, R.; Zang, W.; Tabartehfarahani, A.; Lam, A.; Huang, X.; Sivakumar, A. D.; Thota, C.; Yang, S.; Dickson, R. P.; Sjoding, M. W.; et al. *JAMA Netw. Open* **2023**, *6* (2), No. e230982.
(2) Sharma, R.; Zhou, M.; Tiba, M. H.; McCracken, B. M.; Dickson, R. P.; Gillies, C. E.; Sjoding, M. W.; Nemzek, J. A.; Ward, K. R.; Stringer, K. A.; et al. *ERJ. Open Research* **2022**, *8* (1), 0154−2021.
(3) Shin, J.; Song, J. W.; Flavin, M. T.; Cho, S.; Li, S.; Tan, A.; Pyun, K. R.; Huang, A. G.; Wang, H.; Jeong, S.; et al. *Nature* **2025**, *640* (8058), 375−383.
(4) McCartney, M. M.; Borras, E.; Rojas, D. E.; Hicks, T. L.; Hamera, K. L.; Tran, N. K.; Tham, T.; Juarez, M. M.; Lopez, E.; Kenyon, N. J.; et al. *Commun. Med.* **2022**, *2* (1), 158.
(5) Ghosh, C.; Leon, A.; Koshy, S.; Aloum, O.; Al-Jabawi, Y.; Ismail, N.; Weiss, Z. F.; Koo, S. *Clin. Lab. Med.* **2021**, *41* (2), 185−202.
(6) Aribindi, K.; Linderholm, A.; Borras, E.; Rojas, D. E.; McCartney, M. M.; Davis, C. E.; Harper, R. W.; Kenyon, N. J. *Am. J. Respir. Crit. Care Med.* **2025**, *211* (Abstracts), A5101.
(7) Gordon, A. R.; Lundström, J. N.; Kimball, B. A.; Karshikoff, B.; Sorjonen, K.; Axelsson, J.; Lekander, M.; Olsson, M. J. *Sci. Rep.* **2023**, *13* (1), 16709.
(8) Heng, W.; Yin, S.; Chen, Y.; Gao, W. *IEEE Rev. Biomed. Eng.* **2025**, *18*, 50−73.
(9) Wang, J.; Bryant-Genevier, J.; Nuñovero, N.; Zhang, C.; Kraay, B.; Zhan, C.; Scholten, K.; Nidetz, R.; Buggaveeti, S.; Zellers, E. T. *Microsyst. Nanoeng.* **2018**, *4* (1), 17101.
(10) Fung, S.; Contreras, R. P.; Fung, A. G.; Gibson, P.; Levasseur, M. K.; McCartney, M. M.; Koch, D. T.; Chakraborty, P.; Chew, B. S.; Rajapakse, M. Y.; et al. *J. Chromatogr., A* **2023**, *1705*, 464151.
(11) Rajapakse, M. Y.; Borras, E.; Fung, A. G.; Yeap, D.; McCartney, M. M.; Fabia, F. M.; Kenyon, N. J.; Davis, C. E. *Analyst* **2021**, *146* (2), 636−645.
(12) Blase, R. C.; Libardoni, M. J.; Miller, G. P.; Miller, K. E.; Phillips-Lander, C. M.; Glein, C. R.; Waite, J. H.; Ghosh, A.; Venkatasubramanian, A.; Li, M. W.-H.; et al. *Front. Astron. Space Sci.* **2022**, *9*, 828103.
(13) Cheng, S.-M.; Wang, J.; Wang, Y.-W.; Wei, Z.-B. *ITM Web Conf.* **2017**, *11*, 01019.
(14) Sharma, R.; Zhou, M.; Hunter, M. D.; Fan, X. *J. Agric. Food Chem.* **2019**, *67* (26), 7530−7537.
(15) Borras, E.; Wang, Y.; Shah, P.; Bellido, K.; Hamera, K. L.; Arlen, R. A.; McCartney, M. M.; Portillo, K.; Zhou, H.; Davis, C. E.; et al. *PLoS One* **2023**, *18* (5), No. e0285726.
(16) Wei-Hao Li, M.; Ghosh, A.; Venkatasubramanian, A.; Sharma, R.; Huang, X.; Fan, X. *ACS Sens.* **2021**, *6* (6), 2348−2355.
(17) Narayanan, S.; Rice, G.; Agah, M. *Microchim. Acta* **2014**, *181* (5−6), 493−499.
(18) Zhu, H.; Nidetz, R.; Zhou, M.; Lee, J.; Buggaveeti, S.; Kurabayashi, K.; Fan, X. *Lab Chip* **2015**, *15* (14), 3021−3029.
(19) Li, M. W.-H.; Ghosh, A.; Sharma, R.; Zhu, H.; Fan, X. *Sens. Actuators, B* **2021**, *332*, 129504.
(20) Rezende, G. C.; Le Calvé, S.; Brandner, J. J.; Newport, D. *Micromachines* **2019**, *10* (4), 228.
(21) Freedman, A. N. *J. Chromatogr., A* **1980**, *190* (2), 263−273.
(22) Meyer, M.; Huang, X.; Fan, X.; Kushner, M. J. *J. Appl. Phys.* **2024**, *135* (14), 143301.
(23) Rodríguez-Aguilar, M.; Ramírez-García, S.; Ilizaliturri-Hernández, C.; Gómez-Gómez, A.; Van-Brussel, E.; Díaz-Barriga, F.; Medellín-Garibay, S.; Flores-Ramírez, R. *Biomed. Chromatogr.* **2019**, *33* (12), No. e4684.
(24) Méndez-Rodríguez, K. B.; Figueroa-Vega, N.; Ilizaliturri-Hernandez, C. A.; Cardona-Alvarado, M.; Borjas-García, J. A.; Kornhauser, C.; Malacara, J. M.; Flores-Ramírez, R.; Pérez-Vázquez, F. J. *Biomed. Chromatogr.* **2020**, *34* (12), No. e4956.
(25) Huang, X.; Li, M. W.-H.; Zang, W.; Huang, X.; Sivakumar, A. D.; Sharma, R.; Fan, X. *Microsyst. Nanoeng.* **2022**, *8* (1), 115.
(26) Whiting, J. J.; Myers, E.; Manginell, R. P.; Moorman, M. W.; Anderson, J.; Fix, C. S.; Washburn, C.; Staton, A.; Porter, D.; Graf, D.; et al. *Lab Chip* **2019**, *19* (9), 1633−1643.
(27) Tabata, Y.; Tomita, H. *J. Electrost.* **1990**, *24* (2), 155−166.
(28) Williams, T. *EMC for Product Designers*; Elsevier, 2007; .
(29) Harris, N. R.; Stonard, A. *Proceedings* **2018**, *2*, 705.
(30) Utami, A. M. S.; Syakur, A.; Hermawan, H. *Teknik* **2021**, *42* (1), 10−19.
(31) Glasscott, M. W.; Brown, E. W.; Dorsey, K.; Laber, C. H.; Conley, K.; Ray, J. D.; Moores, L. C.; Netchaev, A. *Anal. Chem.* **2022**, *94* (35), 11983−11989.
(32) Dolgov, B. N.; Forsberg, D. K. Plug-In Photoionization Sensor. U.S. Patent 6,646,444 B2, 2003.
(33) Well, E. Comparing Magnetic and Piezoelectric Transformer Approaches in CCFL Applications. Texas Instruments Inc., 2002. https://www.ti.com/lit/pdf/slyt125 (accessed Sept 2025).
(34) Analog Devices. ADA4530-1. https://www.analog.com/en/products/ada4530-1.html (accessed Sept 2025).

https://doi.org/10.1021/acs.analchem.5c05021
Anal. Chem. 2025, 97, 22397−22406